

# Maxwell's Equations based 3D model of Light Scattering in the Retina

Miriam Santos\*, Adérito Araújo<sup>†</sup>, Sílvia Barbeiro<sup>†</sup>, Francisco Caramelo<sup>‡</sup>, António Correia\*, Maria Isabel Marques<sup>‡</sup>, Miguel Morgado<sup>‡§</sup>, Luís Pinto<sup>†</sup>, Pedro Serranho<sup>‡¶</sup> and Rui Bernardes<sup>‡</sup>

\*AIBILI-Association for Innovation and Biomedical Research on Light and Image, Coimbra, Portugal

<sup>†</sup>CMUC, Department of Mathematics, University of Coimbra, Coimbra, Portugal

<sup>‡</sup>IBILI, Faculty of Medicine, University of Coimbra, Portugal

<sup>§</sup>Department of Physics, University of Coimbra, Portugal, miguelmorgado@uc.pt

<sup>¶</sup>Mathematics Section, Department of Science and Technology, Universidade Aberta, Lisbon, Portugal

**Abstract**—The goal of this work is to develop a computational model of the human retina and simulate light scattering through its structure aiming to shed light on data obtained by optical coherence tomography in human retinas. Currently, light propagation in scattering media is often described by Mie's solution to Maxwell's equations, which only describes the scattering patterns for homogeneous spheres, thus limiting its application for scatterers of more complex shapes. In this work, we propose a discontinuous Galerkin method combined with a low-storage Runge-Kutta method as an accurate and efficient way to numerically solve the time-dependent Maxwell's equations. In this work, we report on the validation of the proposed methodology by comparison with Mie's solution, a mandatory step before further elaborating the numerical scheme towards the propagation of electromagnetic waves through the human retina.

**Index Terms**—Maxwell's equations, Retinal scattering modelling, Optical coherence tomography

## I. INTRODUCTION

The human retina is a multilayered structure in the eye, responsible for the transformation of light energy into neural signals, interpreted by the brain. It is traditionally considered to be composed by ten layers, among which the outer nuclear layer that comprises the cells bodies of light sensitive photoreceptor cells (rods and cones) [1]. Several retinal pathologies, such as diabetic retinopathy, or macular edema, can be detected in their early stages, before noticeable morphologic alterations on the retina [2], by analyzing data acquired through optical coherence tomography (OCT), an imaging technique that uses near infrared light to produce high-resolution images of the retinal tissue [3]. This approach for early diagnosis of retinal conditions is based on functional changes that modify the optical scattering properties of retina, prior to any structural alterations. As OCT standard techniques only provide structural information [4], it is necessary to expand OCT data analysis to account for both structural and functional information. This could be achieved by inverse modeling of

OCT data, using the physical and optical properties of healthy and diseased human retinas and by developing a mathematical model of the respective OCT data [5]. A proper OCT reference for a certain pathology would further enable the identification of the cellular alterations responsible for the observed OCT scans from patients, contributing to an earlier diagnosis and, hopefully, a more efficient treatment.

This research project aims to understand the changes at the cellular level that lead to differences in OCT data, through the solution of the inverse scattering problem, reconstructing the retinal tissues optical properties based on their scattering patterns. For that purpose, the direct scattering problem needs to be assessed, which comprises two main steps (1) the study of the electromagnetic wave propagation and scattering as it travels through the sample and (2) the measurement of scattered light at the detectors [5]. This behaviour of light scattering through the sample can be described by a variety of methods, such as the radiative transfer theory, Lambert's Beer Law, Maxwell's equations and also some statistical approaches using Monte Carlo [5].

Regarding the interaction of electromagnetic field with biological fields, several approaches have been proposed over the past decades, mostly based on single-scattering theory, [7], which cannot fully model the complex structure of the retina. Accounting for such complexity, in particular the variation of the size, shape, refractive indexes and distance between each one of retina's layers, requires a more accurate approach that can be achieved by solving Maxwell's equations [8]. The Mie solution to Maxwell's equations is one of the most popular methods to model tissue scattering at the cellular level [9]. However, Mie's solution only describes the scattering patterns for a single homogeneous sphere, which limits its application to scatterers of different shapes and aggregates of scatterers. The Generalized Multiparticle Mie (GMM) introduced by Xu is an extension of Mie's solution to multiple scattering (aggregates of spheres) [10], that models more accurately light scattering from biological tissues, as assessed by Wang *et al.* [11]. Nevertheless, GMM is also restricted to spherical structures. To describe the scattering phenomena through scatterers of arbitrary shapes, more complex models need to be

studied. The finite-difference time-domain (FDTD) method, first introduced by Yee, is a solution of Maxwell's equations in the time domain, that has been applied to a wide range of electromagnetic problems [12]. In brief, FDTD algorithm starts with Maxwell's curl equations and solves both electric and magnetic fields in time and space rather than describing each one in particular, through a wave equation. Dunn *et al.* pioneered the application of FDTD method to light scattering from cells [13]. This application was further extended by Tanev *et al.* [14] and Su *et al.* [15] to study the influence of different organelles inside the cells. FDTD can model complex structures, namely inhomogeneous objects of arbitrary shapes. However, FDTD method comprise some limitations as well, in particular the computational cost. Due to this, novel techniques have been developed towards Finite Element Methods (FEM) [16]. FEM surpass FDTD methods in terms of geometric flexibility and ability to work with higher orders of accuracy and efficiency in computations.

Our approach encompasses five main steps: (1) development of a Discontinuous Galerkin Finite Element Method (DG-FEM) 3D model of Maxwell's equations, (2) validation of the proposed methodology with Mie's solution for a single spherical scatterer, (3) extension of the method to arbitrary shapes, (4) Monte Carlo simulations of light propagation in the retina, and (5) assessment of the final model's validity for diagnostic and therapeutic purposes. To the best of authors' knowledge, this methodology has never been proposed and applied for a complete inverse modeling of OCT data, thus contributing for an important insight on the understanding of retinal changes at a cellular level.

The present manuscript reports on steps (1) and (2), focusing on the implementation and analysis of DG-FEM Maxwell 3D model by comparison with Mie's theory. The remainder of this paper is organized as follows: Section II outlines the methodological steps used in this work. Section III reports the obtained results and Section IV presents the conclusions and topics of future work.

## II. DG-FEM MAXWELL 3D

In this section, a brief description of DG-FEM Maxwell 3D is presented. We omit a more comprehensive description since it follows the main ideas presented in [8] for the 2D case. Afterwards, the scattering amplitude pattern  $F$ , that allows the computation of macroscopic parameters, anisotropy ( $g$ ) and scattering cross-section ( $\sigma_s$ ), comparable to Mie's solution, is achieved.

### A. Discontinuous Galerkin method

The DG formulation used in this work follows the nodal formulation described [18] and its specifications were previously discussed, for the 2D case, in [8]. Now we consider the 3D case and restrict our attention to computational domains (meshes) tessellated by tetrahedrons. A sample mesh used in the work is shown in Fig. 1.

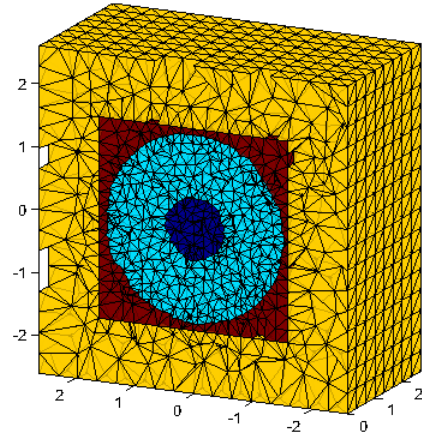


Fig. 1. One sample of a surface mesh for a sphere with a cubic domain.

### B. Low-storage Runge-Kutta

For the time integration we used the improved fourth-order, 14-stage low-storage Runge-Kutta (LSRK) presented in [19] instead of the fourth-order, five-stage LSRK method considered in [18]. This modification has proven to reduce the computational time in 40%, without further increasing the computational cost, as corroborated in [8].

### C. Domain constraints and specifications

In electromagnetic simulation, and even more for the successful application of the DG method, it is important to account for boundary conditions, frequently known as absorbing boundary conditions. The purpose of specifying such constraints is to avoid undesirable reflections caused by non-absorbing boundary conditions, that invade the simulation domain and interfere with the observation of the phenomenon of interest. We consider the perfectly matched layer (PML) formulation in [20]. Furthermore, to simulating the full complexity of the retina, a variable permittivity was introduced, changing the initial formulations in [18].

### D. Variable Permittivity

Since we are modelling exclusively biological domains, which are magnetically transparent, the magnetic permeability will be considered as a constant ( $\mu \simeq 1$ ). To introduce the effect of spatially variable electric permittivity ( $\epsilon \rightarrow \epsilon(x)$ ), the numerical fluxes ( $\mathbf{E}$  and  $\mathbf{H}$ ) must incorporate the local impedance  $Z$  and conductance  $Y$  as  $Z^\pm = \frac{1}{Y^\pm} = \sqrt{\frac{1}{\epsilon^\pm}}$ , where the superscript “+” refers to the neighbouring element and the superscript “-” refers to the local cell.

### E. Near-To-Far-Field Transformation

Providing a well-defined scattered-field region enables the computation of the near-field scattering pattern. However, to simulate the retina's layers, we're interested in the far-field scattering phenomena. Using the near-field data, it is possible to use a near-field to far-field transformation (NTFFT) to

obtain the far-field scattering pattern [21]. The NTFFFT is an application of the surface equivalence principle: the values of the near-field at a virtual surface surrounding the scatterer can be used to compute a magnetic and electric “current” that allows the computation of the scattered field at any point outside the virtual surface. Accordingly, the near-field time-domain values are converted to frequency-time values with a discrete Fourier transform, and the equivalent phasor electric current  $\vec{J}_s$  and equivalent magnetic current  $\vec{M}_s$  are defined on the surface  $S$ , as follows from [21]. The NTFFFT is succinctly explained in [21] and we shall simply sketch the most relevant steps for the far-field pattern calculation. Using  $\mathbf{J} = \nabla \times \mathbf{H}$ ,  $\mathbf{M} = -\nabla \times \mathbf{E}$  and  $\Psi = x \sin \theta \cos \phi + y \sin \theta \sin \phi + z \cos \theta$ , the angular dependent components are given by:

$$\begin{aligned} N_\theta &= \iint_S (J_x \cos \theta \cos \phi + J_y \cos \theta \sin \phi - J_z \sin \theta) e^{ik\Psi} ds \\ N_\phi &= \iint_S (-J_x \sin \phi + J_y \cos \phi) e^{ik\Psi} ds \\ L_\theta &= \iint_S (M_x \cos \theta \cos \phi + M_y \cos \theta \sin \phi - M_z \sin \theta) e^{ik\Psi} ds \\ L_\phi &= \iint_S (-M_x \sin \phi + M_y \cos \phi) e^{ik\Psi} ds \end{aligned} \quad (1)$$

$$N_\phi = \sum_{i=1}^K \iint_{S^k} (-J_x \sin \phi + J_y \cos \phi) e^{ik(x \sin \theta \cos \phi + y \sin \theta \sin \phi + z \cos \theta)} ds \quad (2)$$

$$= \sum_{i=1}^K J_k \int_{-1}^1 \int_{-1}^{-t} (-J_x \sin \phi + J_y \cos \phi) e^{ik(x(\eta) \sin \theta \cos \phi + y(\eta) \sin \theta \sin \phi + z(\eta) \cos \theta)} d\eta \quad (3)$$

$$= \sum_{i=1}^K J_k \sum_{l=1}^{N_c} w_l (-J_x^l \sin \phi + J_y^l \cos \phi) e^{ik(x^l \sin \theta \cos \phi + y^l \sin \theta \sin \phi + z^l \cos \theta)} \quad (4)$$

Finally, knowing  $N_\theta, N_\phi, L_\theta$  and  $L_\phi$ , the far-field scattering pattern,  $F_s(\theta, \phi)$  is defined by

$$F_s(\theta, \phi) = \frac{k^2}{32\pi^2 r^2 P_{inc}} (|L_\phi + N_\theta|^2 + |L_\theta - N_\phi|^2) \quad (5)$$

where  $r$  is a point in the far-field and  $\theta$  and  $\phi$  are the angles measured from the  $z$  and  $x$  axes in spherical coordinates.  $F_s(\theta, \phi)$  represents the scattered intensity at any point in the far-field, and allows the computation of the macroscopic parameters  $g$  and  $\sigma_s$ , as

$$g = \int_0^\pi p(\theta) \cos(\theta) \sin(\theta) d\theta \quad (6)$$

$$\sigma_s = \int_0^{2\pi} \int_0^\pi F_s(\theta, \phi) \sin(\theta) d\theta \quad (7)$$

where  $p(\theta)$  is scattering phase function, obtained according to [13].

Since  $S$  is a surface composed of non-overlapping, connecting triangular elements, we can change the integrals in (1) to integrals on the mesh elements' domain in order to be able to numerically evaluate them using gaussian cubature. Here, we decompose the tetrahedral elements into triangle elements, describing each element's face in 2D coordinates. Each element was rotated to make their faces parallel to the  $xy$  axis, discarding the  $z$  component. This allows the computation of 2D Vandermonde matrices and the creation of an interpolation matrix between the reference element nodes and the cubature nodes [22]. After obtaining the cubature nodes and interpolating the field components to these nodes, the element is re-rotated to its original position. An example is given for  $N_\phi$  (see equations (2) to (4)). The mesh elements are rotated and mapped to the standard triangle defined as  $I = \{\mathbf{r} = (r, s) | (r, s) \geq -1; r + s \leq 0\}$  from (2) to (3), resulting in the transformation Jacobian  $J_k$  and integration limit change. Then, the rotation applied to the general element map is applied in reverse to the cubature mapping, thus obtaining the cubature mapping in the face's original position. Using gaussian cubature of order  $N_c$ , (3) may be evaluated as (4), considering that all phasors are already interpolated to the cubature nodes,  $l$ , on the triangular element's surface.

### III. RESULTS

The validation of DG-FEM Maxwell 3D with Mie's solution, requires a simplification of the retinal layers' model. The layers are assumed to be composed by spherical cells, following the assumptions of Mie's theory. In fact, a single spherical cell is considered, simply modelled as a dielectric object. Two sets of domain parameters are required: one that complies straightforward with Mie's solution and one that follows the principles of DG-FEM Maxwell 3D. Table I resumes the two sets of input parameters. For Mie's solution, a software based on [23]. For DG-FEM, all mesh generation is done with [24]. Before each simulation, the initial mesh is discretized as a cube domain,  $\Omega$ , with two spherical interfaces, which correspond to the spherical scatterer and the surrounding virtual surface where the field's dynamics are collected.

For unpolarized light only, the differential scattering cross sections  $d\sigma/d\theta$ , solely depending on the scattering angle (azimuthally averaged) were calculated. The comparison between Mie's and DG-FEM Maxwell 3D solution was done

TABLE I  
MIE'S AND DG-FEM MAXWELL 3D INPUT PARAMETERS

Input Parameters		
Mie's solution	Sphere Diameter	1
	Refractive Index of the medium	1
	Refractive Index of the sphere	$1.5 + 0j$
	Wavelength in Vacuum	1
Maxwell's solution	Medium radius	1.5
	PML limits	1.6

by calculating the differential cross sections and the relative percentual error between the  $g$  and  $\sigma_s$  results, according to equations (8) and (9). The results are shown in Figures 2 and 3 and Table III.

$$\delta g = \frac{|g_{Mie} - g_{DG-FEM}|}{g_{Mie}} \times 100 \quad (8)$$

$$\delta \sigma_s = \frac{|\sigma_{sMie} - \sigma_{sDG-FEM}|}{\sigma_{sMie}} \times 100 \quad (9)$$

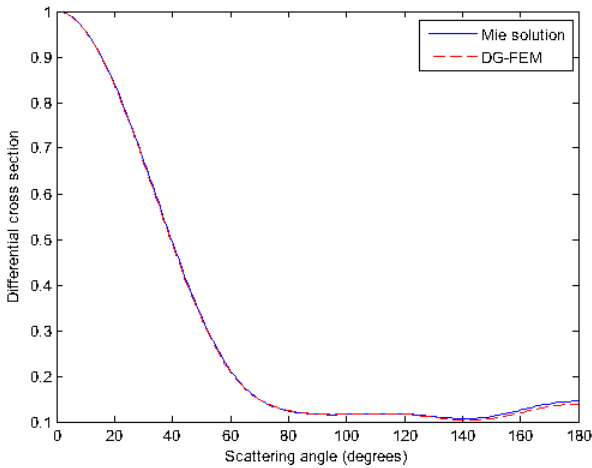


Fig. 2. Normalized plot of  $d\sigma/d\theta$  for all scattering angles between 0 and 180° degrees.

TABLE II  
COMPARISON OF  $g$  AND  $\sigma_s$  FOR BOTH SOLUTIONS.

	$g$	$\sigma_s$
Mie's solution	0,72924	2,7367
DG-FEM simulation	0,73193	2,7349
Relative error (%)	0,36794	0,064

The obtained results are within the required precision for biological domains. However, some aspects need further improvement, mostly regarding the sensibility to the incident wave's frequency, DG-FEM order of interpolation and mesh discretization. Our simulations have shown that an increase in the wave's frequency requires an increase in the method's

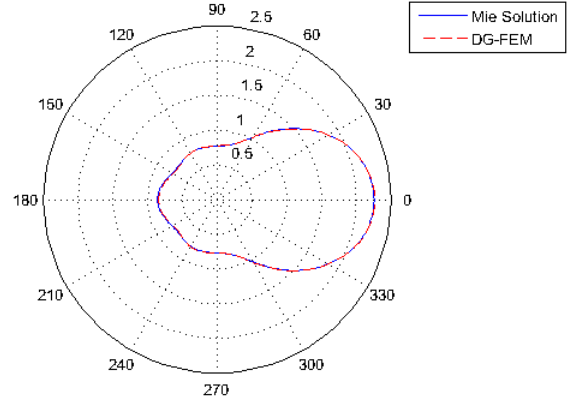


Fig. 3. Polar plot of  $d\sigma/d\theta$  for all scattering angles between 0 and 360° degrees.

order, which is computationally expensive. Furthermore, the quality of the mesh also affects the precision of results and cannot be compensated by increasing the polynomial order. In order to improve the mesh quality and precision while maintaining a reasonable computational time could be the further refinement of the mesh in areas where the electromagnetic fields are expected to be more complex. Further developments of the DG-FEM method will account for this susceptibilities.

#### IV. CONCLUSIONS

In this paper, we proposed a method for solving the time-dependent Maxwell's equations focusing on the simulation of light scattering through the retina's layers, DG-FEM Maxwell 3D. The validation of the proposed methodology was done by comparison with Mie's theory, considering the light scattering for a single sphere, using the same parameters as inputs for both models. The obtained results are in agreement with those obtained using Mie's theory, with small percentage differences of 0.37% and 0.06% for the scattering anisotropy ( $g$ ) and scattering cross-section ( $\sigma_s$ ), respectively. This validation was a mandatory step prior to further elaborating the numerical scheme towards the propagation of electromagnetic waves through structures with more complex shapes present in the human retina. The successful validation of our methodology removes Mie's dependence from the final model, enables the extrapolation of the method to the human eye's structures and allows the computation of parameters required by larger scale simulations, using Monte Carlo methods. Furthermore, the proposed approach enables the simulation of larger domains, e.g. the full retina, without the computational burden associated with the Maxwell numerical solver.

#### ACKNOWLEDGMENTS

This work was supported by the AIBILI - Association for Innovation and Biomedical Research on Light and Image, IBILI - Institute for Biomedical Imaging and Life Sciences and

Centro de Matemática da Universidade de Coimbra (CMUC), funded by the European Regional Development Fund through the program COMPETE, and by the Portuguese Government through the FCT - Fundação para a Ciência e a Tecnologia under the projects PEst-C/MAT/UI0324/2013, PEST-C/SAU/UI3282/2013 and PTDC/SAU-ENB/119132/2010.

## REFERENCES

- [1] L. Junqueira and J. Carneiro, *Basic Histology: Text & Atlas (Junqueira's Basis Histology)*, McGraw-Hill Medical, 2005.
- [2] R. Bernardes, P. Serranho, T. Santos, V. Goncalves and J. Cunha-Vaz, "Optical Coherence Tomography: automatic retina classification through support vector machines," *European Ophthalmic Review*, 2012; 6:4:200-203.
- [3] P. Serranho, A. M. Morgado and R. Bernardes, *Optical Coherence Tomography: a concept review*, *Optical Coherence Tomography: A Clinical and Technical Update*. R. Bernardes and J. Cunha-Vaz, Eds. Berlin - Heidelberg: Springer-Verlag, 2012; 139-156.
- [4] J. A. Schliesser, G. Gallimore, N. Kunjukunju, N. R. Sabates, P. Koulen and F. N. Sabates, "Clinical application of optical coherence tomography in combination with functional diagnostics: advantages and limitations for diagnosis and assessment of therapy outcome in central serous chorioretinopathy," *Clinical Ophthalmology (Auckland, N.Z.)* 2014;8:2337-2345. doi:10.2147/OPHT.S73119.
- [5] P. Elbau, L. Mindrinos and O. Scherzer, "Mathematical modelling of optical coherence tomography," arXiv:1403.0726, 2014.
- [6] A. Correia, L. Pinto, A. Araújo, S. Barbeiro, F. Caramelo, P. Menezes, M. Morgado, P. Serranho and R. Bernardes, "Monte Carlo simulation of diabetic macular edema changes on optical coherence tomography data," *IEEE EMBS International Conferences on Biomedical and Health Informatics*, Valencia, Spain, 2014; 724,727. doi: 10.1109/BHL.2014.686446.
- [7] J. M. Schmitt, A. Knüttel and R. F. Bonner, "Measurement of optical properties of biological tissues by low-coherence reflectometry," *Appl. Opt.* 1993;32:6032-6042.
- [8] A. Araújo, S. Barbeiro, L. Pinto, F. Caramelo, A. Correia, M. Morgado, P. Serranho, A. S. C. Silva, and R. Bernardes, "Numerical solution of time-dependent Maxwell's equations for modeling scattered electromagnetic wave's propagation," *Proceedings of the 13th International Conference on Computational and Mathematical Methods in Science and Engineering*, CMMSE 2013, 2013.
- [9] S. L. Jacques, "Optical properties of biological tissues: a review," *Phys Med Biol.* 2013;58(11):R37-61. doi: 10.1088/0031-9155/58/11/R37.
- [10] Y. Xu, "Electromagnetic scattering by an aggregate of spheres," *Appl. Opt.* 1995; 34(21):4573-4588.
- [11] M. Wang, M. Cao, Z. R. Guo and G. U. Ning, "Generalized multi-particle Mie modeling of light scattering by cells," 2013, 58: 2663?2666, doi: 10.1007/s11434-013-5719-0.
- [12] K. Yee, "Numerical solutions of initial boundary value problems involving Maxwell's equations in isotropic media," *IEEE Trans. Antennas Propagat.*, 1966;AP-14:302-307.
- [13] A. Dunn and R. Richards-Kortum, "Three-dimensional computation of light scattering from cells," *IEEE J. Sel. Top. Quantum Electron.* 1996; 898-905.
- [14] S. Tabev, W. B. Sun, J. Pond, V. V. Tuchin and V. P. Zharov, "Flow cytometry with gold nanoparticles and their clusters as scattering contrast agents: FDTD simulation of light-cell interaction," *J Biophotonics*, 2009, 2: 505?520.
- [15] X. T. Su, K. Singh, W. Rozmus, C. Backhouse and C. Capjack, "Light scattering characterization," *Opt Express*, 2009, 17:13381?13388.
- [16] U. S. Inan and R. A. Marshall, *Numerical Electromagnetics: the FDTD method*, Cambridge: Cambridge University Press, 2011.
- [17] W. Reed and T. Hill, *Triangular mesh methods for the neutron transport equation*, Los Alamos Scientific Laboratory, LA-UR-73-479, 1973.
- [18] J. Hesthaven and T. Warburton, *Nodal discontinuous Galerkin methods: algorithms, analysis and applications*, Springer Verlag, New York, 2008.
- [19] J. Niegemann, R. Diehl and K. Bush, "Efficient low-storage Runge-Kutta schemes with optimized stability regions", *J. Comput. Phys.*, 2012; 231:364-372.  
J. Niegemann, M. König, K. Stannigel and K. Bush, "Higher-order time-domain methods for the analysis of nano-photonics systems," *Phot. Nano. Fund. Appl.*, 2009; 7:2-11.
- Z. S. Sacks, D. M. Kingsland, R. Lee and J. F. Lee, "A perfectly matched anisotropic absorber for use as an absorbing boundary condition", *IEEE Trans. Antennas Propagat.*, 1995; 43:1460-1463.
- M. König, K. Bush and J. Niegemann, "The discontinuous Galerkin time-domain method for Maxwell's equations with anisotropic materials," *Phot. Nano. Fund. Appl.*, 2010; 8:303-309.
- [20] E. Turkel and A. Yefet, "Absorbing PML boundary layers for wave-like equations," *Applied Numerical Mathematics*, 1998;27:533-557.
- [21] A. Taflove and S. C. Hagness, *Computational Electrodynamics: the finite-difference time-domain method*, Artech House, ISBN 978-1580538329, 2005.
- [22] V. Olshevsky and E. Tyrtyshnikov, *Matrix Methods: Theory, Algorithms and Applications*, World Scientific, ISBN 978-9812836021, 2014.
- [23] J. Schäfer, S. Lee and A. Kienle, "Calculation of the near fields for the scattering of electromagnetic waves by multiple infinite cylinders at perpendicular incidence," *J. Quant. Spectrosc. Radiat. Trans.* 113(16), 2012.
- [24] [www.freefem.org/ff++/](http://www.freefem.org/ff++/)